Gold nanoparticle size and shape effects on cellular uptake and intracellular distribution of siRNA nanoconstructs

Jun Yue[†], **Timothy Joel Feliciano**[†], **Wenlong Li**[§], **Andrew Lee**[#], and **Teri W. Odom**[†,‡,*]

[†]Department of Chemistry, Northwestern University, Evanston, Illinois 60208, United States

[#]Department of Chemical and Biological Engineering, Northwestern University, Evanston, Illinois 60208, United States

[‡]Department of Materials Science and Engineering, Northwestern University, Evanston, Illinois 60208, United States

[§]School of Materials Science and Engineering, Nanyang Technological University, 639798, Singapore

Abstract

Gold nanoparticles (AuNPs) show potential for transfecting target cells with small interfering RNA (siRNA), but the influence of key design parameters such as the size and shape of the particle core is incomplete. This paper describes a side-by-side comparison of the *in vitro* response of U87 glioblastoma cells to different formulations of siRNA-conjugated gold nanoconstructs targeting the expression of isocitrate dehydrogenase 1 (IDH1) based on 13-nm spheres, 50-nm spheres, and 40-nm stars. 50-nm spheres and 40-nm stars showed much higher uptake efficiency compared to 13-nm spheres. Confocal fluorescence microscopy showed that all three formulations were localized in the endosomes at early incubation times (2 h) but that after 24 h, 50-nm spheres and 40-nm stars were neither in endosomes nor lysosomes while 13-nm spheres remained in endosomes. Transmission electron microscopy images revealed that the 13-nm spheres were enclosed and dispersed within endocytic vesicles while 50-nm spheres and 40-nm stars were aggregated, and some of these NPs were outside of endocytic vesicles. In our comparison of nanoconstructs with different sizes and shapes, while holding siRNA surface density and nanoparticle concentration constant, we found that larger particles (50-nm spheres and 40-nm stars) showed higher potential as carriers for the delivery of siRNA.

TOC graphic

---

[*]Corresponding Author: todom@northwestern.edu.

13-nm spheres   50-nm spheres   40-nm stars

200 nm

20 μm
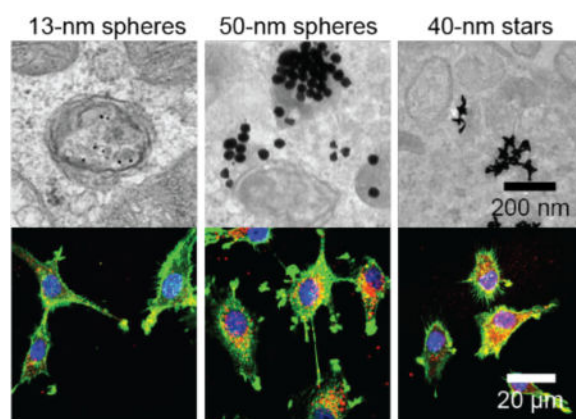
Keywords

Gold nanoparticles; gold nanostars; siRNA nanoconstructs; confocal microscopy; transmission electron microscopy; cellular uptake; intracellular distribution

INTRODUCTION

Glioblastoma multiforme (GBM) is the most common and aggressive form of malignant primary brain tumors and has one of the poorest survival rates (14–16 months) after diagnosis.[1] Isocitrate dehydrogenase 1 (IDH1) has been recognized as a metabolic target for the development of small interfering RNA (siRNA)-based therapies against GBM.[2, 3] However, the use of siRNA as a therapeutic agent requires carriers for delivery and stabilization against nuclease degradation.[4] Gold nanoparticles (AuNPs) can serve as potential siRNA carriers[5] since "free" siRNA can be chemically conjugated and presented by the particle cores at high surface densities. AuNP-siRNA conjugates have been shown to enter cells through scavenger receptor A-mediated endocytosis and to knock down gene expression *in vitro* and *in vivo*.[6–10] When densely packed on the surface of spherical AuNPs, siRNA is more resistant to nuclease degradation compared to their free forms.[11, 12] Further development of AuNPs as siRNA delivery agents for therapeutic applications requires an understanding of a critical biological property: cellular uptake and subsequent trafficking within cells, particularly to the cytosol (the location of the RNA-induced silencing complex).[13–15]

Structural features of nanoconstructs that influence cellular uptake include size, shape, and surface chemistry.[16, 17] Size-dependent cellular uptake has been observed in a variety of spherical AuNPs,[18–21] but consensus for an optimal size to maximize levels of cellular uptake has not been reached. While studies of citrate-capped or protein-functionalized AuNPs have shown that 50-nm AuNPs led to the greatest uptake by cervical cancer cells (HeLa),[18, 19] AuNPs functionalized with the drug tiopronin showed that ultra-small NPs (2 nm) showed the greatest cellular uptake by breast cancer cells (MCF-7).[20] Such contrasting observations indicate that uptake also depends on the type of biomolecules presented by the AuNP surface and interactions with cell-surface receptors. Other properties of NPs, such as

PEGylation, surface charge, and the formation of protein coronas *in vitro* and *in vivo* also influence cellular uptake.[21–23]

NP shape is an additional structural feature that can influence uptake.[18, 24–26] For example, gold nanorods showed lower uptake efficiency compared to spherical particles, with the rate of cellular uptake decreasing with increasing aspect ratio.[18] Gold nanostars (AuNS), anisotropic NPs having multiple branches, have shown efficient delivery of magnetic resonance imaging T_1 contrast agents *in vitro*; these high relaxivity Gd (III)-DNA AuNS showed significant contrast enhancement over their spherical counterparts.[27] Furthermore, AuNS have shown great potential as carriers for the delivery of therapeutic aptamers in a variety of cancer cell lines.[28–30] However, an evaluation of the biological properties of AuNS and spherical AuNPs functionalized with oligonucleotides to determine the effects of particle shape has not yet been performed. Moreover, although a range of NP-siRNA conjugates has been tested as siRNA delivery vehicles,[31] a side-by-side comparison of cellular uptake and intracellular distribution of AuNP-siRNA conjugates that vary in size and shape is needed to accelerate the design of these nanoconstructs.

Here we compare the *in vitro* biological properties of siRNA nanoconstructs (NP-siRNA) with different siRNA surface densities and different AuNPs cores: 13-nm and 50-nm Au spheres and 40-nm Au stars. We tested nine combinations of cores and ligand surface densities and found that NP size and shape not only influenced the kinetics of cellular uptake but also affected intracellular distribution. At short times (up to 8 h), each nanoconstruct formulation was taken up by human primary glioblastoma U87 cells in similar amounts based on the number of internalized AuNPs. At longer periods of time (16–24 h), however, cellular uptake was greater for 50-nm spheres and 40-nm stars (with greatest uptake by 50-nm spheres) compared to 13-nm spheres. These higher uptake levels for 50-nm spheres and 40-nm stars were correlated with changes in cell morphology and differences in subcellular localization. Confocal fluorescence microscopy and immunostaining of the subcellular compartments showed that after 24 h, 13-nm sphere siRNA conjugates remained in endosomes, while most of the 50-nm spheres and 40-nm star carriers were neither localized to endosomes nor lysosomes. TEM images provided improved insight to the confocal images, and we found that 50-nm-sphere and 40-nm-star conjugates within cells were often aggregated and in many instances, outside of endocytic vesicles.

RESULTS AND DISCUSSION

Preparation of NP-siRNA Nanoconstructs with Different Sizes and Shapes

To compare effects of size and shape, we prepared NP-siRNA nanoconstructs with different particle cores (13-nm spheres, 50-nm spheres and 40-nm stars) (Figure 1a) but with comparable siRNA surface densities. AuNPs were functionalized with thiol-terminated siRNA and mercaptoundecyl hexa(ethylene glycol) (EG_6) (Figure 1b) according to literature.[32] In brief, we synthesized NP-siRNA constructs by adding siRNA to citrate-capped Au spheres (13-nm and 50-nm) and HEPES-capped Au stars in a NaCl solution (Experimental Procedures). We used a model siRNA sequence specific for IDH1, which is a potential therapeutic gene target for GBM[33] consisting of double-stranded RNA with a 3'-thiol group on the "sense" oligonucleotide strands and several 2'-OCH_3 groups in both the

"sense" and "antisense" oligonucleotides, to increase the resistance of siRNA to nuclease activity. The addition of EG_6 following the conjugation of siRNA passivated the Au surface, which not only prevented aggregation of NP-siRNA during synthesis and purification, but also displaced remaining citrate (13-nm and 50-nm spheres) or HEPES (40-nm nanostars) from the AuNP surfaces.[34]

Previous work has shown that oligonucleotide-functionalized spherical AuNPs can enter cells through receptor-mediated endocytosis, which involves the multivalent binding of oligonucleotide to scavenger receptors.[35, 36] Because the surface density of oligonucleotides is a key parameter for cellular uptake,[37] we compared AuNP-siRNA constructs with similar siRNA surface densities. We quantified the number of antisense (AS) and sense (S) strands by selectively dissociating the oligonucleotides from the AuNP surfaces and then analyzing OliGreen fluorescence, a nonspecific intercalator of single-stranded oligonucleotides (Experimental Procedures). Next, we tuned the loading of RNA strands by adjusting the molar ratio of siRNA added to AuNPs (R). To prevent NP aggregation during the salt-aging process, a minimum R was required for 13-nm spheres (200:1), 50-nm spheres (1200:1) and 40-nm stars (1200:1), respectively. Figure 2 shows that loading of RNA strands increased with increased R, and a maximum loading of RNA strands was achieved when R was higher than 800 for 13-nm spheres or 3200 for 50-nm spheres and 40-nm stars.

Table 1 summarizes the chemical and physical properties of siRNA nanoconstructs. Notably, the stoichiometry of AS oligonucleotides per NP (those hybridized to the sense strand) was lower than that of the sense oligonucleotides (bound to the Au surface at the 3'-thiol group) for all three formulations. This observation is consistent with previous work on 13-nm AuNP-siRNA[32] and indicates partial dehybridization during adsorption and purification steps.[32] We chose to compare NP-siRNA that were similar in surface density of total oligonucleotide (S and AS strands per NP or per nm^2) since this property is hypothesized to contribute to the physico-chemical properties and cellular uptake of NP-siRNA constructs.[35] After functionalization, hydrodynamic diameters of NP-siRNA constructs increased by a comparable extent (12–22 nm). All three formulations had negative surface charge and similar zeta potential values, which ensured a similar surface chemical environment for comparison.

Uptake of NP-siRNA by U87 Cells: Influence of Size and Shape

The cellular uptake of NP-siRNA constructs was evaluated in a model cancer cell line U87, a grade IV GBM cell line with high levels of expression of IDH1. Before incubation with NP-siRNA constructs, U87 cells were grown for a time longer than that of the doubling time (34 h) until > 80% confluence was achieved to minimize the influence of cell-cycle on the uptake.[38] To quantify NP cellular uptake, we used inductively coupled mass spectrometry (ICP-MS) to determine the gold content per cell. Using a two-dimensional projection of AuNPs from TEM images to estimate particle volume,[39] we converted Au content (number of atoms) to number of AuNPs per cell. To examine the effect of NP size, we compared 13-nm spheres (23 ± 8 AS per NP) with 50-nm spheres (329 ± 42 AS per NP); these structures had similar surface density of total RNA (~ 0.16 molecules nm^{-2}). We treated U87 cells (2×10^4 cells per well in a 24-well plate) with NP-siRNA constructs under the same

concentration of NP (0.5 nM) in Dulbecco's Modified Eagle Medium (DMEM) supplemented with 10% FBS. The siRNA concentration under these conditions was greater for 50-nm spheres than for 13-nm spheres by a factor of ~14. We treated cells with these nanoconstructs at equivalent concentrations of NPs instead of siRNA because we aimed to understand the cellular recognition and entry of the nanostructures based on size and shape.

Figure 3a shows that uptake of 13-nm spheres and 50-nm spheres was comparable over the first 8 h of incubation with ca. 10^4 particles per cell for each NP-siRNA. Note that total siRNA uptake was 10-fold greater for 50-nm spheres than for 13-nm spheres because of the greater surface area and siRNA stoichiometry per particle. Furthermore, cellular uptake of NP-siRNA constructs accelerated for 50-nm spheres after this period (2 h and 8 h), which ultimately resulted in cellular uptake levels greater than those of 13-nm spheres by a factor of 3.6, and a corresponding level of siRNA delivery that was greater by 50-fold after 24 h.

To investigate the effect of NP shape, we compared 50-nm spheres (221 ± 34 AS per NP) to 40-nm stars (251 ± 41 AS per NP) with similar surface densities of overall RNA (0.13 molecules nm^{-2}). Figure 3b indicates that cellular uptake of spherical NPs increased at a higher rate compared to the nanostars, and uptake efficiency of the 50-nm spheres at 24 h was 1.6 times higher than that of 40-nm stars. Although the uptake levels of NP-siRNA with different shapes were similar in the first 8 h of incubation (~8×10^3 particles per cell), major differences in cellular uptake emerged at later time points. Since the siRNA density and hydrodynamic diameter of these constructs were comparable, we hypothesized that the greater uptake of spheres over that of stars may be attributed to differences in interactions between oligonucleotides presented by spherical surfaces and those from branches directed by nanostars and cell membrane-class A scavenger receptors implicated in the uptake of oligonucleotides presented by spherical NPs.[36] To determine whether NP-siRNA constructs entered U87 cells by scavenger-receptor-mediated endocytosis, we investigated uptake of NP-siRNA by U87 cells pre-treated with polyinosinic acid (poly(I), an inhibitor that can bind with scavenger receptors and thus block scavenger-receptor-mediated endocytosis). Pre-treatment of U87 cells with poly(I) resulted in a reduction of cellular uptake: 53% (for 13-nm spheres), 54% (for 50-nm spheres) and 63% (for 40-nm stars) (Supporting Information, Figure S2), which support that scavenger receptors play an important role in cellular uptake of NP-siRNA. Taken together, the results indicate (1) distinct increases in cellular uptake of NPs driven by an increase in particle size; (2) a dependence on NP shape, where uptake of spherical particles was greater than that of nanostars of comparable surface area; and (3) the rates of cellular uptake increased after an initial 8-h period for larger particles, which is different from uptake kinetics previously reported for 13-nm AuNP-oligonucleotide conjugates, where the most rapid uptake occurred within the first 60 min.[40]

Uptake of NP-siRNA by U87 Cells: Influence of RNA Density

To determine how the loading density of RNA strands on NPs affected uptake, we quantified the cellular uptake of NP-siRNA constructs under three different surface RNA densities. The range of surface density of siRNA for 13-nm spheres (0.16–0.6 molecules nm^{-2}) is higher than 50-nm spheres (0.07–0.16 molecules nm^{-2}) and 40-nm stars (0.06–0.19 molecules nm^{-2}) (Table 1) because of large differences of surface curvature. Therefore, we

independently tested density effects on cellular uptake for each formulation. Figure 4 shows cellular uptake with varying surface densities of RNA strands. For 13-nm spheres, when the density of RNA strands increased from 0.16 to 0.44 molecules nm^{-2}, cellular uptake increased by 28%, while decreased uptake was observed when the density was further increased to 0.60 molecules nm^{-2}. Previous work has shown that polyvalent interactions between single-stranded DNA 13-nm spherical AuNPs (ssDNA-AuNP) and scavenger receptors on cell membranes determined the cell uptake efficiency of ssDNA-AuNPs, with higher ssDNA densities leading to increased cellular uptake.[35]

This discrepancy may be due to the different surface compositions (ssDNA *vs.* siRNA) of the AuNPs. For 50-nm spheres and 40-nm stars, we found that the trend of cellular uptake *vs.* RNA density followed that of 13-nm spheres, where the median density of total RNA showed the highest cellular uptake efficiency. One explanation for the decrease in levels of cellular uptake at the highest surface densities may be from steric effects and reduced accessibility of siRNA to interact with scavenger receptors. Surface densities at which cellular uptake decreased were considerably higher for NP-siRNA with 13-nm spheres (0.6 molecules nm^{-2}) compared with 50-nm spheres and 40-nm stars and may be due to differences of surface curvature. Literature on targeting systems, where NP constructs enter cells by receptor-mediated endocytosis, have shown that overcrowding of ligands on the NP surface prevent ligands from obtaining the correct orientation necessary for binding to receptors.[41] These results also indicate that size and shape of NP-siRNA have a stronger influence on cellular uptake at longer incubation times (24 h) compared to surface loading density. At the 24-h point, larger 50-nm spheres demonstrated the highest average uptake of ca. 5.4×10^4 NPs/cell, while 40-nm nanostars had slightly less uptake (~3.4×10^4 NPs/cell), and 13-nm spheres showed the lowest uptake of ca. 1.9×10^4 NPs/cell.

Intracellular distribution of NP-siRNA constructs

To visualize NP-siRNA within U87 cells, we prepared NP-siRNA functionalized with single-stranded DNA (dT_{20} with a 3'-thiol) labelled with 5'-Cy5 (dT_{20}-Cy5) for analysis by confocal laser scanning microscopy. During the functionalization process, we pre-mixed dT_{20}-Cy5 with siRNA (molar ratio 1:8) before adding to the AuNP solution and assumed that the relatively small amount of dT_{20}-Cy5 would not adversely influence the final surface composition of NP-siRNA constructs. We analyzed the surface composition of nanoconstructs functionalized with siRNA and dT_{20}-Cy5, and indeed found that their loading of total RNA (AS and S strands) were not significantly different from those of without dT_{20}-Cy5. The proportion of dT_{20}-Cy5 strands to the siRNA oligonucleotides was small and similar among three formulations (5.5%, 4.7% and 4.4% for 13-nm spheres, 50-nm spheres and 40-nm stars, respectively). To test whether the addition of dT_{20}-Cy5 perturbed the cellular uptake of NP-siRNA, we compared the cellular uptake of nanoconstructs with dT_{20}-Cy5 to those without dT_{20}-Cy5 by ICP-MS. We found cellular uptake of NP-siRNA/Cy5 compared to unlabeled constructs was enhanced by 40%, 54% and 33% for 13-nm spheres, 50-nm spheres and 40-nm stars respectively (Supporting Information, Figure S3), which may be from the small fraction of oligonucleotides presenting positively charged Cy5 at the AuNP surfaces. However, the data showed similar trends on cellular uptake (greatest uptake efficiency for 50-nm spheres, followed by 40-nm

stars, followed by 13-nm spheres), which suggests that the Cy5 labels did not change the nature of the interaction of the NP-siRNA with U87 cells.

Next, we monitored the cellular uptake of three formulations of Cy5-labeled nanoconstructs with similar density of RNA strands (0.21, 0.19 and 0.18 molecules nm^{-2} for 13-nm spheres, 50-nm spheres and 40-nm stars, respectively) by confocal microscopy at two representative time points (2 h and 24 h), corresponding to the two major regimes found in the kinetic analysis of Figure 3. Figure 5a shows U87 cells following the incubation with NP-siRNA/Cy5 at an equivalent NP concentration for the three formulations or the equivalent volume of PBS as control. At equal concentrations of NPs, the levels of siRNA and Cy5 for the 50-nm spheres and 40-nm stars were ca. 12 and 9-fold greater than that of 13-nm spheres. To distinguish whether nanoconstructs were internalized by cells or just associated within the extracellular matrix (ECM), we stained the actin cytoskeleton with phalloidin, which can differentiate between intracellular compartments and the ECM. At short time periods (2 h), the Cy5 fluorescence was surrounded by actin signals, which supported that NP-siRNA were distributed inside cells. At longer incubation times (24 h), we found that U87 cells showed significant accumulation of 50-nm spheres and 40-nm stars and lower levels for 13-nm spheres. In a separate experiment, we treated U87 cells with NP-siRNA with equivalent concentrations of siRNA and Cy5 and also observed higher levels of Cy5 within cells treated with 50-nm spheres or 40-nm stars compared to 13-nm spheres (Supporting Information, Figure S4). Both quantitative analysis of AuNP uptake (Figure 3) and qualitative analysis of Cy5 fluorescence confirmed that larger NP-siRNA constructs entered U87 cells in greater amounts (on a particle-to-particle basis) and are more efficient carriers for delivering siRNA.

Interestingly, we discovered differences in cell morphology among the different formulations at both time points of observation (2 and 24 h) (Figure 5a). Cells treated with 13-nm spheres had long, narrow, branched extensions like control cells treated with PBS, while cells treated with 50-nm spheres and 40-nm stars showed fewer structures of this type. To investigate whether changes in cell morphology were induced by possible toxicity of nanoconstructs, we tested the viability of U87 cells by 2-(4-sulfophenyl)-2H-tetrazolium (MTS) assay after treatments with the same concentrations of NP-siRNA/Cy5 used in the confocal studies (Experimental Procedures). Figure 5b shows that the cell viabilities following treatment with all three NP-siRNA were greater than 80%, which suggested minimal cytotoxicity.

Endocytotic processes may involve the rearrangement (assembly and disassembly) of actin filaments, leading to reshaping of the plasma membrane and facilitation of internalization.[42, 43] To test whether the morphological changes of U87 cells were correlated with cellular uptake of NP-siRNA, we pre-treated U87 cells with an actin polymerization inhibitor (cytochalasin D, CytoD) and then investigated the cellular uptake of the three NP-siRNA in the presence of CytoD. Figure 5c shows that inhibition of actin polymerization resulted in the inhibition of cellular uptake of NP-siRNA, and that the magnitude depended on NP size and shape. Cellular uptake of 13-nm spheres showed only a minor decrease (~10%) in uptake in cells with arrested polymerization, while 50-nm spheres and 40-nm stars showed greater levels of inhibition (20–30%). These observations suggest (1) that

endocytosis of 50-nm spheres and 40-nm stars involve greater levels of actin polymerization compared to 13-nm stars; and (2) that the morphological changes observed in U87 cells from 50-nm spheres and 40-nm stars may be related to cytoskeletal rearrangements and actin polymerization involved in the endocytosis of these constructs.

Subcellular Localization of NP-siRNA

Besides cellular uptake, the subcellular location of nanoconstructs is another critical parameter that can influence therapeutic efficacy and especially for siRNA, delivery of the constructs to the cytoplasm is needed. One challenge for NP-based constructs is that following endocytosis, the majority of nanoconstructs reside in early endosomes, and from there are sorted to late endosomes and lysosomes.[44] To investigate the subcellular trafficking of NP-siRNA and the dependence of trafficking on the size and shape of NP-siRNA, we treated U87 cells with three different formulations of NP-siRNA/Cy5 and monitored their localization. Using antibodies targeting the early endosome antigen 1 (EEA1) and lysosome-associated membrane glycoprotein 1 (LAMP1), we labeled the endosomes and lysosomes with different fluorophores to establish independently the co-localization of NP-siRNA with endosomes and lysosomes.

Figure 6 shows confocal microscopy images of NP-siRNA/Cy5 constructs in U87 cells at two time points (2 h and 24 h). At 2 h, nearly all the construct signals, regardless of NP size and shape, overlapped well with endosomal signals (representative areas indicated by solid yellow arrows), which suggests that NP-siRNA constructs first localize in endosomes. There is no significant overlap of Cy5 fluorescence with lysosomes at this early incubation time. As the incubation time increased to 24 h, the location of NP-siRNA constructs within U87 cells varied among the three formulations. For 13-nm spheres, only a small amount of signal overlapped with lysosomal signals (solid white arrows, Figure 6), and most of the NP-siRNA constructs remained trapped within endosomes. For 50-nm spheres, most of the nanoconstructs showed little co-localization with either endosomes or lysosomes (hollow white arrows, Figure 6). 40-nm stars showed distributions like the 50-nm spheres with only slight differences in intracellular distribution. Taken together, the results indicate that NP-siRNA constructs follow the endosomal pathway at the beginning of endocytosis (within 2 h) but that over long incubation times (24 h), the 13-nm spheres remained in endosomes while 50-nm spheres and 40-nm stars were in neither early endosomes nor lysosomes.

To test whether 50-nm spheres and 40-nm star constructs were distributed in the cytoplasm, we visualized their intracellular location with transmission electron microscopy (TEM) after 24 h (Figure 7). To increase the contrast of the cellular organelles, we double-stained cell sections by uranyl acetate and lead citrate (Experimental Procedures). For cells treated with 13-nm spheres, nearly all the NPs were enclosed by a clear, intact membrane (Figure 7a), indicating that 13-nm spheres were trapped in vesicles. Within the vesicles, 13-nm spheres were well separated. For cells treated with 50-nm spheres however, many NPs were found outside the vesicles (Figure 7b, yellow arrows). We also observed 50-nm spheres trapped in vesicles, which appeared as large aggregates of particles. Correlating this data with confocal images in Figure 6, we suggest that the vesicles are endocytic compartments other than early endosomes or lysosomes. Interestingly, some vesicle membranes enclosing the 50-nm

spheres were not well resolved compared to those around 13-nm spheres, and some membranes seemed to be locally disrupted and discontinuous (Figure 7b, orange arrows). In U87 cells treated with 40-nm stars, we also observed stars outside of vesicles (Figure 7c, yellow arrows), while those that remained trapped in vesicles appeared as NP aggregates with very few isolated NPs. Figure S5 summarizes a more extensive set of TEM images of U87 cells treated with NP-siRNA that further support these observations.

Previous TEM work has indicated a wide range of intracellular distributions of AuNPs, most likely because of differences in the nanoconstructs (for example, size/shape of AuNPs and surface functionalization), cell type, and culture conditions.[45] We have summarized the literature in Table S3 (Supporting Information). For example, citrate or polyethylene glycol coated 15-nm spherical AuNPs were mainly distributed in vesicles in human alveolar epithelial cells (A549); vesicle sizes containing NPs increased from less than 150 nm to greater than 1000 nm as incubation time increased from 1 h to 24 h.[46] In contrast, similarly sized spherical AuNPs functionalized with cell-penetrating peptides showed unusual distribution in HeLa cells, where AuNPs were initially (2 h) found in the cytosol, nucleus, and mitochondria but were later (24 h) found densely packed within vesicles and then finally distributed into the cytosol after even longer periods of time (48 h).[47] For NP-siRNA, we found that subcellular distribution most strongly depended on size, where 13-nm spheres were only found in vesicles, and 50-nm spheres and 40-nm stars were found in vesicles and in the cytoplasm.

CONCLUSION

In summary, we examined the influence of the structural features of NP diameter and NP shape on the ability of NP-siRNA to enter U87 cells. We fabricated nine formulations of siRNA conjugated Au nanoconstructs based on cores of 13-nm spheres, 50-nm spheres and 40-nm stars. Using a set of techniques (quantitative analysis of AuNPs and fluorescence and electron microscopy imaging of dye-labelled oligonucleotides and AuNPs), we differentiated the cellular response and the intracellular distribution of the NP-siRNA. Side-by-side comparison of cellular uptake of the formulations indicated much higher uptake efficiency for 50-nm spheres and 40-nm stars compared to 13-nm NPs. By means of confocal fluorescence microscopy, we found all the formulations were localized in the endosomes at an early incubation time (2 h); however, after 24 h, a majority of 50 nm spheres and 40-nm stars were neither in endosomes nor in lysosomes, while 13-nm spheres remained in the endosomes. Interestingly, we found that 50-nm spheres and 40-nm stars formed clusters within cells, and to some extent were distributed to the cytoplasm, while 13-nm spheres were mainly distributed inside the vesicles in a form of single NP. These observations indicate that the size of AuNPs is a major design feature that can influence uptake of siRNA (from greater numbers of NPs as well greater amounts of siRNA delivered per particle) and that the intracellular distribution of the larger NP-siRNA can be differentiated from that of smaller NPsiRNA. The underlying cause for these differences, as well as the consequences on the function of siRNA delivered by NPs, requires further study. Larger NP diameters in the design of NP-siRNA should be considered as a key feature in the development of NP agents for *in vitro* and potentially *in vivo* delivery of siRNA.

EXPERIMENTAL PROCEDURES

Synthesis of siRNA Conjugated Gold Nanoconstructs

Spherical AuNPs with 13-nm diameter were synthesized by reducing chloroauric acid ($HAuCl_4$) in sodium citrate solution. Spherical AuNPs with 50-nm diameter were obtained from Ted Pella. Gold nanostars (AuNS) were synthesized by reducing 0.2 mM of $HAuCl_4$ at room temperature in 110 mM of HEPES buffer (Atlanta Biologicals). To prepare duplex siRNA, the sense strand (3'-dTdTU$_{OMe}$U$_{OMe}$U$_{OMe}$GC$_{OMe}$C$_{OMe}$C$_{OMe}$U$_{OMe}$AU$_{OMe}$AGAU$_{OMe}$ACU$_{OMe}$G$_{OMe}$U$_{OMe}$-5', 200 μM) and anti-sense strand (5'-AAACGGGAU$_{OMe}$AU$_{OMe}$C$_{OMe}$U$_{OMe}$AU$_{OMe}$GAC$_{OMe}$AdTdT -3', 200 μM) were hybridized in nuclease-free duplex buffer (30 mM HEPES and 100 mM potassium acetate, pH 7.5, IDT). The hybridization was carried out by first heating the solution to 45 °C for 15 min, then cooling to 37 °C over 30 min and 4 °C for another 30 min. Duplex siRNA was added to the AuNP solution at a molar ratio of 200 for 13-nm spheres and 1200 for 50-nm spheres and AuNS. SDS was then added to the reaction mixture to a final concentration of 5 mM, and the mixture was shaken at room temperature for 2 h to allow the adsorption of siRNA on NP surface. NaCl was added to the mixture, while shaking, to result in a sequence of increasing concentrations of NaCl in the reaction mixtures for the following time periods: (1) 50 mM for 1h; (2) 100 mM for 1 h; (3) 200 mM for 1 h; (4) 400 mM for 16 h. Subsequently, 11-mercaptoundecyl hexa(ethylene glycol) (EG$_6$, Aldrich) was added to the mixture at a molar ratio (to AuNP) of 2000 for 13-nm spheres and 10,000 for 50-nm spheres and AuNS. The mixture was shaken at room temperature for 5 h, followed by centrifugation at 4 °C using different speeds for different NPs (13-nm spheres: 21,000 ×g for 30 min; 50-nm spheres: 8000 ×g for 10 min AuNS: 9000 ×g for 10 min). The supernatant was discarded and the pellet was resuspended in nuclease-free PBS buffer (Thermo). Two more centrifugation cycles were carried out to completely remove the unconjugated siRNA and EG$_6$.

Quantifying Number of Sense and Anti-sense Strands on NPs

To determine the stoichiometry of the RNA oligonucleotide to AuNP, the noncovalently associated anti-sense strands and covalently conjugated sense strands were sequentially separated from the AuNPs. Gold nanoconstructs (2×10^{-12} mol) were suspended in 400 μL of 8 M urea and heated to 45 °C with shaking for 20 min. The solution was diluted with 0.1% Tween-20 to a final concentration of 4 M urea and centrifuged, followed by the separation of the supernatant solution, containing AS oligonucleotides, and AuNP pellet. The AuNP pellet was re-suspended in 10 μL of iodine solution (0.16 M I_2 and 1.0 M KI) and the mixture was shaken at room temperature for 5 min, followed by addition of 10 μL of 1.0 M NaH_2PO_4. Reaction with $NaBH_4$ and dithiothreitol (DTT) (1 : 5 mixture of 2 M $NaBH_4$: 0.3 M DTT) for 5 min was followed by centrifugation at 21,000 ×g for 10 min to obtain a supernatant containing sense strands. The concentrations of antisense strands (C_{AS}) and sense strands (C_S) in each supernatant were analyzed by the Quant-iT OliGreen (Invitrogen) assay, where OliGreen reagent was added to the supernatant for measurements of the fluorescence at λ_{ex} = 485 nm. A calibration curve was generated using reaction mixtures containing AuNPs and standards of C_{AS} or C_S, prepared in parallel and with the same

chemical reactions used to dissociate AS and S from the nanoconstructs. Finally, the number of anti-sense strands (or sense strands) per AuNP was calculated by dividing C_{AS} or C_S by the concentration of AuNPs which was measured by ICP-MS.

Cellular Uptake of Nanoconstructs

The human primary glioblastoma cell line U87 (ATCC) maintained in Dulbecco's Modified Eagle's medium (DMEM) (Gibco) supplemented with 10% fetal bovine serum (FBS) (Gibco) was used as the target cell line for *in vitro* efficiency evaluations. Cells were plated on 12-well plates with the density of 2×10^4 cells / well and cultured in complete growth media at 37 °C with 5% CO_2 until cells reached ~80% confluence. Cells were treated with 0.5 nM of gold nanoconstructs for different time periods (2 h, 8 h, 16 h, and 24 h), after which the supernatant was removed and cells were washed 3 times with PBS. Cells were then treated with trypsin to release the cells from the plates. Trypsinized cells were transferred to a 1.5 mL of Eppendorf tube and washed 3 times with PBS by centrifugation at 300 $g \times 5$ min. After washing, cell pellets were resuspended in PBS and counted with a hemocytometer. Finally, cells were treated with an acid solution (2% HCl + 2% HNO_3) at 70 °C overnight to prepare lysates for the quantification of gold by inductively coupled plasma mass spectrometry (ICP-MS).

Confocal Imaging of Cy5-labeled Nanoconstructs

To visualize the NP distributions within cells, all the three formulations were backfilled with 5'-Cy5-conjugated $(dT)_{20}$ oligonucleotides with 3'-disulfide. U87 cells were plated on a round coverslip ($d = 12$mm, BD Biosciences) with the density of 10^4 cells / coverslip and cultured in complete growth media overnight. Cells were treated with 0.5 nM of Cy5-labeled nanoconstructs for 2 h or 24 h, followed by 3-time washing with PBS. Cells were fixed with 4% paraformaldehyde at room temperature for 10 min, washed 3 times with PBS, permeabilized with Triton X100 (0.1%, at room temperature for 5 min), and then washed 3 times again with PBS. The actin cytoskeleton of permeabilized cells was stained with Alexa Fluor® 594 Phalloidin at room temperature for 30 min. Finally, the coverslips were mounted on glass slides using DAPI-containing ProLong™ antifade mounting medium (Invitrogen).

Immunofluorescence Staining

After plating on the coverslips, cells were treated with Cy5-labeled 13-nm, 50-nm or AuNS nanoconstructs which had the similar density of RNA strands (0.21, 0.19 and 0.18 molecules nm^{-2} for 13-nm spheres, 50-nm spheres and 40-nm stars, respectively). After 2 h or 24 h incubation, the coverslips were washed 3 times with PBS, fixed with 4% paraformaldehyde and permeabilized with 0.1% Triton X100. Cells were incubated with the blocking solution (1% BSA and 10% rabbit serum in PBS) at room temperature for 1 h. Cells were then incubated at 4 °C overnight with a solution of primary antibodies (mouse anti-human LAMP-1 antibody and goat anti-human EEA-1 antibody; 300-fold dilutions of stocks from Santa Cruz Biotechnology) in blocking solution. After overnight incubation, coverslips were washed 6 times with PBST (0.1% Tween 20 in PBS) over 1 h. Secondary antibodies (rabbit anti-mouse IgG (H + L) Alexa Fluor 488 and rabbit antigoat IgG (H + L) Alexa 594, Thermo) in blocking solution were incubated with the cells for 1 h at room temperature.

Following an additional 6 washes with PBST buffer over 1 h, coverslips were mounted on glass slides using DAPI-containing antifade mounting medium (Invitrogen).

TEM Imaging of Nanoconstructs Taken up by U87 Cells

U87 cells were seeded in a 12-well plate with the density of 4×10^5 cells / well. After 48 h, cells were incubated with 0.5 nM of NP-siRNA nanoconstructs in DMEM supplemented with 10% FBS for 24 h at 37 °C in 5% CO_2. Cells were then washed with PBS for 3 times and harvested by treating with 0.25% trypsin-EDTA for 5 min at the room temperature. The cells were then centrifuged at $300 \times g$ for 5 min. The supernatant was removed, and the pellets were transferred to the Karnovsky's fixative and fixed using a Pelco Biowave microwave for 4 min. Primary fixative was exchanged for fresh fixative, and microwave fixation was carried out for another 4 min, followed by two washes with phosphate buffer (PB). A subsequent fixation step was carried out with the secondary fixative of 1% osmium tetroxide in DI water, followed by 3 washes with DI water. A series of acetone solutions (30%, 50%, 70%, 90% in DI water), followed by 2 treatments with 100% acetone was used to dehydrate the specimens. Cells were then infiltrated with 25% and 50% of EMBed 812 resin with microwaving, followed by bench infiltration with 75% of resin in acetone overnight. Two further infiltrations with 100% resin were carried out over 5 h. Polymerization took place in a 60 °C oven for 24 h. A Leica Ultracut S or RMC MT-6000 XL microtome was used to collect 90 nm thick sections. Cell sections were double-stained with uranyl acetate and lead citrate. Finally, imaged were captured by a JEOL1230 TEM and Gatan 831 bottom-mounted CCD camera.

Supplementary Material

Refer to Web version on PubMed Central for supplementary material.

## Acknowledgments

References

1. Sturm D, Bender S, Jones DT, Lichter P, Grill J, Becher O, Hawkins C, Majewski J, Jones C, Costello JF, et al. Paediatric and adult glioblastoma: multiform (epi)genomic culprits emerge. Nat Rev Cancer. 2014; 14:92–107. [PubMed: 24457416]

2. Galluzzi L, Kepp O, Vander Heiden MG, Kroemer G. Metabolic targets for cancer therapy. Nat Rev Drug Discov. 2013; 12:829–46. [PubMed: 24113830]

3. Nam WS, Park KM, Park JW. RNA interference targeting cytosolic NADP(+)-dependent isocitrate dehydrogenase exerts anti-obesity effect in vitro and in vivo. Biochim Biophys Acta. 2012; 1822:1181–8. [PubMed: 22542506]

4. Sakurai Y, Hatakeyama H, Sato Y, Hyodo M, Akita H, Harashima H. Gene silencing via RNAi and siRNA quantification in tumor tissue using MEND, a liposomal siRNA delivery system. Mol Ther. 2013; 21:1195–203. [PubMed: 23568259]

5. Lytton-Jean AK, Langer R, Anderson DG. Five years of siRNA delivery: spotlight on gold nanoparticles. Small. 2011; 7:1932–7. [PubMed: 21681985]

6. Cutler JI, Auyeung E, Mirkin CA. Spherical nucleic acids. J Am Chem Soc. 2012; 134:1376–91. [PubMed: 22229439]

7. Giljohann DA, Seferos DS, Daniel WL, Massich MD, Patel PC, Mirkin CA. Gold nanoparticles for biology and medicine. Angew Chem Int Ed Engl. 2010; 49:3280–94. [PubMed: 20401880]

8. Ding Y, Jiang Z, Saha K, Kim CS, Kim ST, Landis RF, Rotello VM. Gold nanoparticles for nucleic acid delivery. Mol Ther. 2014; 22:1075–83. [PubMed: 24599278]

9. Pissuwan D, Niidome T, Cortie MB. The forthcoming applications of gold nanoparticles in drug and gene delivery systems. J Control Release. 2011; 149:65–71. [PubMed: 20004222]

10. Kim HJ, Takemoto H, Yi Y, Zheng M, Maeda Y, Chaya H, Hayashi K, Mi P, Pittella F, Christie RJ, et al. Precise engineering of siRNA delivery vehicles to tumors using polyion complexes and gold nanoparticles. ACS Nano. 2014; 8:8979–91. [PubMed: 25133608]

11. Seferos DS, Prigodich AE, Giljohann DA, Patel PC, Mirkin CA. Polyvalent DNA nanoparticle conjugates stabilize nucleic acids. Nano Lett. 2009; 9:308–11. [PubMed: 19099465]

12. Rosi NL, Giljohann DA, Thaxton CS, Lytton-Jean AK, Han MS, Mirkin CA. Oligonucleotide-modified gold nanoparticles for intracellular gene regulation. Science. 2006; 312:1027–30. [PubMed: 16709779]

13. Paroo Z, Liu Q, Wang X. Biochemical mechanisms of the RNA-induced silencing complex. Cell Res. 2007; 17:187–94. [PubMed: 17310219]

14. Oh YK, Park TG. siRNA delivery systems for cancer treatment. Adv Drug Deliv Rev. 2009; 61:850–62. [PubMed: 19422869]

15. Williford JM, Wu J, Ren Y, Archang MM, Leong KW, Mao HQ. Recent advances in nanoparticle-mediated siRNA delivery. Annu Rev Biomed Eng. 2014; 16:347–70. [PubMed: 24905873]

16. Zhang S, Gao H, Bao G. Physical Principles of Nanoparticle Cellular Endocytosis. ACS Nano. 2015; 9:8655–71. [PubMed: 26256227]

17. Dykman LA, Khlebtsov NG. Uptake of engineered gold nanoparticles into mammalian cells. Chem Rev. 2014; 114:1258–88. [PubMed: 24279480]

18. Chithrani BD, Ghazani AA, Chan WC. Determining the size and shape dependence of gold nanoparticle uptake into mammalian cells. Nano Lett. 2006; 6:662–8. [PubMed: 16608261]

19. Chithrani BD, Chan WC. Elucidating the mechanism of cellular uptake and removal of protein-coated gold nanoparticles of different sizes and shapes. Nano Lett. 2007; 7:1542–50. [PubMed: 17465586]

20. Huang K, Ma H, Liu J, Huo S, Kumar A, Wei T, Zhang X, Jin S, Gan Y, Wang PC, et al. Size-dependent localization and penetration of ultrasmall gold nanoparticles in cancer cells, multicellular spheroids, and tumors in vivo. ACS Nano. 2012; 6:4483–93. [PubMed: 22540892]

21. Cho EC, Au L, Zhang Q, Xia Y. The effects of size, shape, and surface functional group of gold nanostructures on their adsorption and internalization by cells. Small. 2010; 6:517–22. [PubMed: 20029850]

22. Jiang Y, Huo S, Mizuhara T, Das R, Lee YW, Hou S, Moyano DF, Duncan B, Liang XJ, Rotello VM. The Interplay of Size and Surface Functionality on the Cellular Uptake of Sub-10 nm Gold Nanoparticles. ACS Nano. 2015; 9:9986–93. [PubMed: 26435075]

23. Maiorano G, Sabella S, Sorce B, Brunetti V, Malvindi MA, Cingolani R, Pompa PP. Effects of cell culture media on the dynamic formation of protein-nanoparticle complexes and influence on the cellular response. ACS Nano. 2010; 4:7481–91. [PubMed: 21082814]

24. Cho EC, Zhang Q, Xia Y. The effect of sedimentation and diffusion on cellular uptake of gold nanoparticles. Nat Nanotechnol. 2011; 6:385–91. [PubMed: 21516092]

25. Bartczak D, Muskens OL, Nitti S, Sanchez-Elsner T, Millar TM, Kanaras AG. Interactions of human endothelial cells with gold nanoparticles of different morphologies. Small. 2012; 8:122–30. [PubMed: 22102541]

26. Wang Y, Black KC, Luehmann H, Li W, Zhang Y, Cai X, Wan D, Liu SY, Li M, Kim P, et al. Comparison study of gold nanohexapods, nanorods, and nanocages for photothermal cancer treatment. ACS Nano. 2013; 7:2068–77. [PubMed: 23383982]

27. Rotz MW, Culver KS, Parigi G, MacRenaris KW, Luchinat C, Odom TW, Meade TJ. High relaxivity Gd(III)-DNA gold nanostars: investigation of shape effects on proton relaxation. ACS Nano. 2015; 9:3385–96. [PubMed: 25723190]

28. Dam DH, Culver KS, Odom TW. Grafting aptamers onto gold nanostars increases in vitro efficacy in a wide range of cancer cell types. Mol Pharm. 2014; 11:580–7. [PubMed: 24422969]

29. Dam DH, Lee JH, Sisco PN, Co DT, Zhang M, Wasielewski MR, Odom TW. Direct observation of nanoparticle-cancer cell nucleus interactions. ACS Nano. 2012; 6:3318–26. [PubMed: 22424173]

30. Lee H, Dam DH, Ha JW, Yue J, Odom TW. Enhanced Human Epidermal Growth Factor Receptor 2 Degradation in Breast Cancer Cells by Lysosome-Targeting Gold Nanoconstructs. ACS Nano. 2015; 9:9859–67. [PubMed: 26335372]

31. Conde J, Ambrosone A, Hernandez Y, Tian FR, McCully M, Berry CC, Baptista PV, Tortiglione C, de la Fuente JM. 15 years on siRNA delivery: Beyond the State-of-the-Art on inorganic nanoparticles for RNAi therapeutics. Nano Today. 2015; 10:421–450.

32. Barnaby SN, Lee A, Mirkin CA. Probing the inherent stability of siRNA immobilized on nanoparticle constructs. Proc Natl Acad Sci U S A. 2014; 111:9739–44. [PubMed: 24946803]

33. Stegh AH. IDH1 promotes tumor growth and resistance to targeted therapies in the absence of mutation. Cancer Research. 2016; 76

34. Jans H, Stakenborg T, Jans K, Van de Broek B, Peeters S, Bonroy K, Lagae L, Borghs G, Maes G. Increased stability of mercapto alkane functionalized Au nanoparticles towards DNA sensing. Nanotechnology. 2010; 21:285608. [PubMed: 20585165]

35. Patel PC, Giljohann DA, Daniel WL, Zheng D, Prigodich AE, Mirkin CA. Scavenger receptors mediate cellular uptake of polyvalent oligonucleotide-functionalized gold nanoparticles. Bioconjug Chem. 2010; 21:2250–6. [PubMed: 21070003]

36. Choi CH, Hao L, Narayan SP, Auyeung E, Mirkin CA. Mechanism for the endocytosis of spherical nucleic acid nanoparticle conjugates. Proc Natl Acad Sci U S A. 2013; 110:7625–30. [PubMed: 23613589]

37. Giljohann DA, Seferos DS, Patel PC, Millstone JE, Rosi NL, Mirkin CA. Oligonucleotide loading determines cellular uptake of DNA-modified gold nanoparticles. Nano Lett. 2007; 7:3818–21. [PubMed: 17997588]

38. Kim JA, Aberg C, Salvati A, Dawson KA. Role of cell cycle on the cellular uptake and dilution of nanoparticles in a cell population. Nat Nanotechnol. 2011; 7:62–8. [PubMed: 22056728]

39. Dam DH, Lee RC, Odom TW. Improved in vitro efficacy of gold nanoconstructs by increased loading of G-quadruplex aptamer. Nano Lett. 2014; 14:2843–8. [PubMed: 24689438]

40. Narayan SP, Choi CH, Hao L, Calabrese CM, Auyeung E, Zhang C, Goor OJ, Mirkin CA. The Sequence-Specific Cellular Uptake of Spherical Nucleic Acid Nanoparticle Conjugates. Small. 2015; 11:4173–82. [PubMed: 26097111]

41. Elias DR, Poloukhtine A, Popik V, Tsourkas A. Effect of ligand density, receptor density, and nanoparticle size on cell targeting. Nanomedicine. 2013; 9:194–201. [PubMed: 22687896]

42. Samaj J, Baluska F, Voigt B, Schlicht M, Volkmann D, Menzel D. Endocytosis, actin cytoskeleton, and signaling. Plant Physiol. 2004; 135:1150–61. [PubMed: 15266049]

43. Kukulski W, Schorb M, Kaksonen M, Briggs JA. Plasma membrane reshaping during endocytosis is revealed by time-resolved electron tomography. Cell. 2012; 150:508–20. [PubMed: 22863005]

44. Canton I, Battaglia G. Endocytosis at the nanoscale. Chem Soc Rev. 2012; 41:2718–39. [PubMed: 22389111]

45. Levy R, Shaheen U, Cesbron Y, See V. Gold nanoparticles delivery in mammalian live cells: a critical review. Nano Rev. 2010; 1

46. Brandenberger C, Muhlfeld C, Ali Z, Lenz AG, Schmid O, Parak WJ, Gehr P, Rothen-Rutishauser B. Quantitative evaluation of cellular uptake and trafficking of plain and polyethylene glycol-coated gold nanoparticles. Small. 2010; 6:1669–78. [PubMed: 20602428]

47. Krpetic Z, Saleemi S, Prior IA, See V, Qureshi R, Brust M. Negotiation of intracellular membrane barriers by TAT-modified gold nanoparticles. ACS Nano. 2011; 5:5195–201. [PubMed: 21609028]
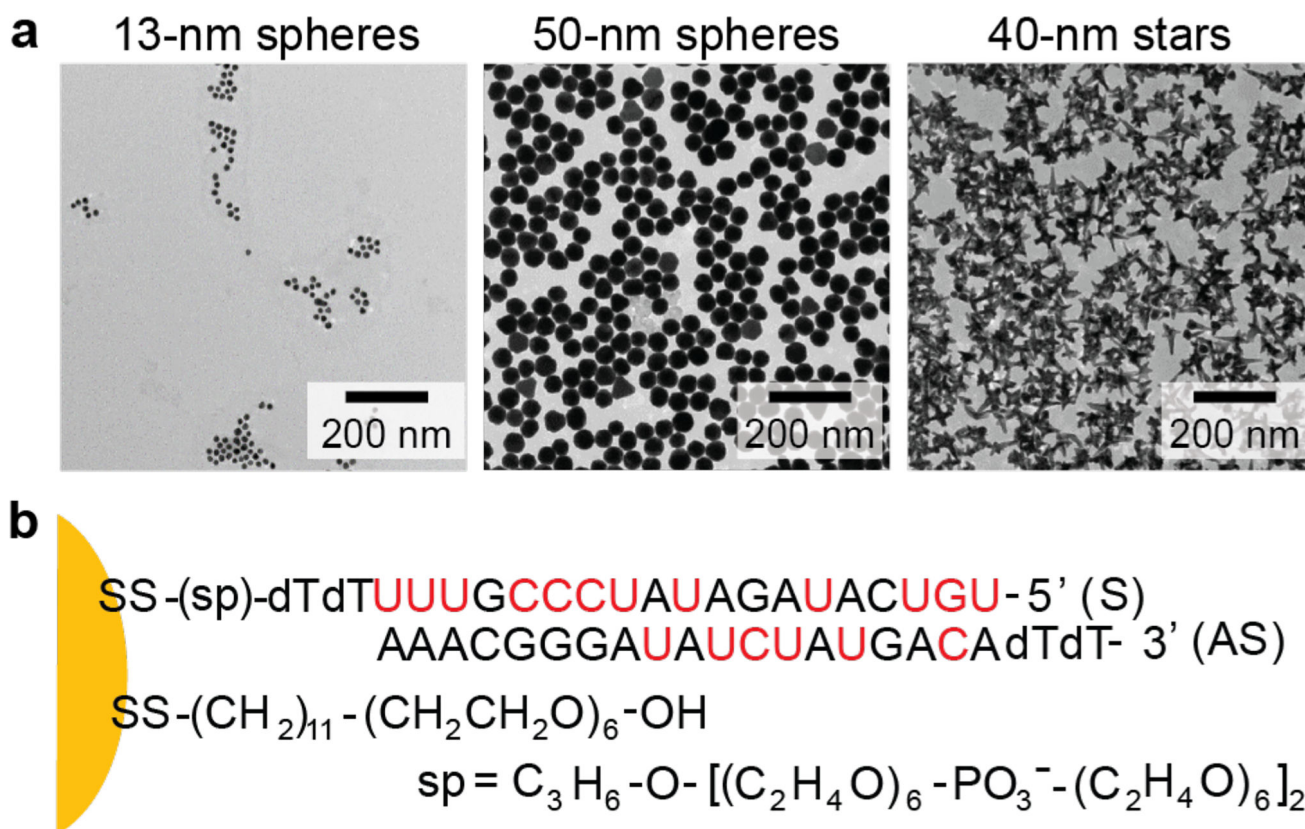
Figure 1. Composition of core-shell structures of NP-siRNA constructs
(a) Transmission electron microscopy (TEM) images of Au NP cores. **(b)** Chemical composition of the ligand shell. Nucleotides highlighted in red have 2'-OCH$_3$ substitutions to increase their resistance to nuclease-catalyzed degradation.
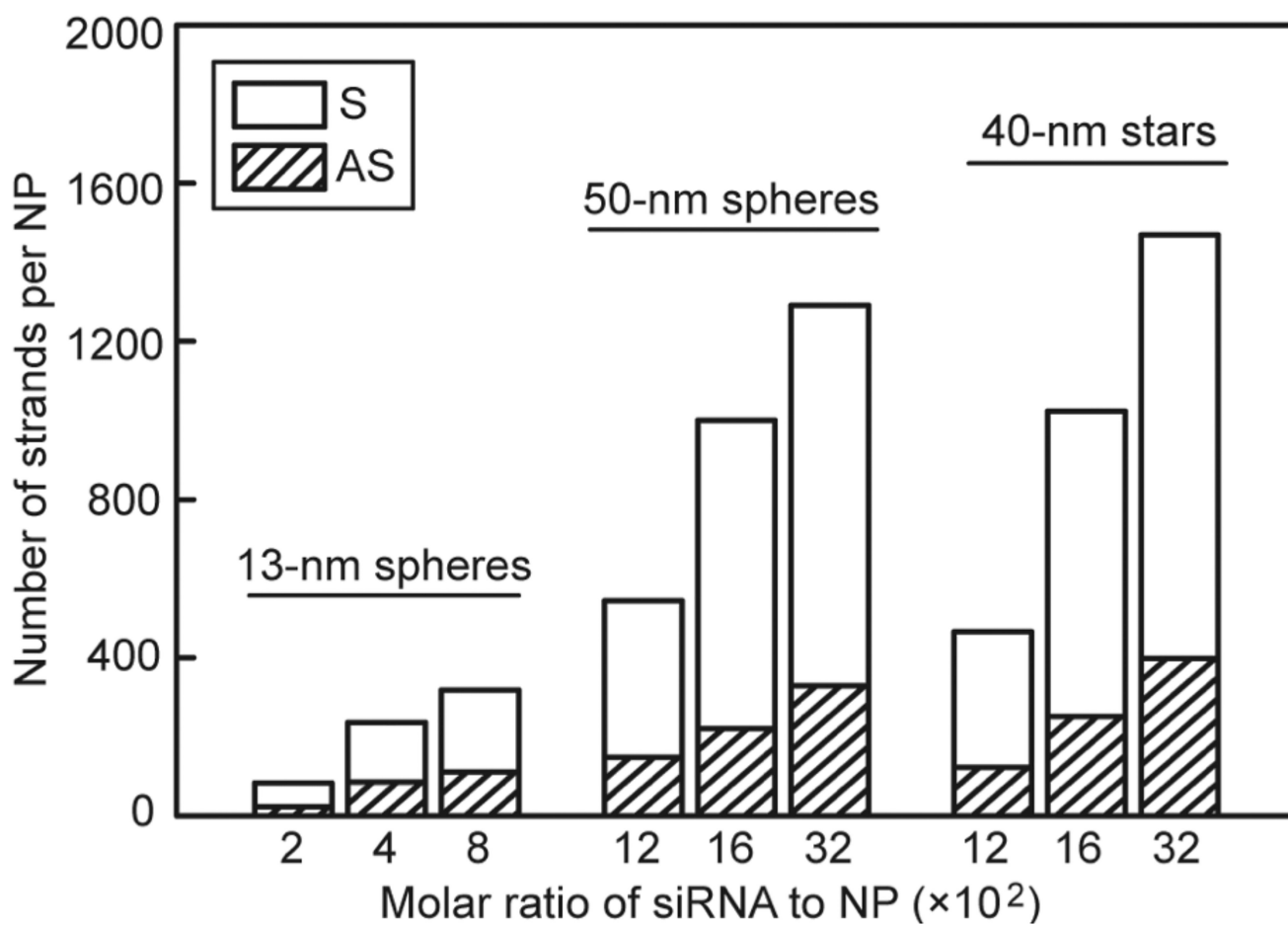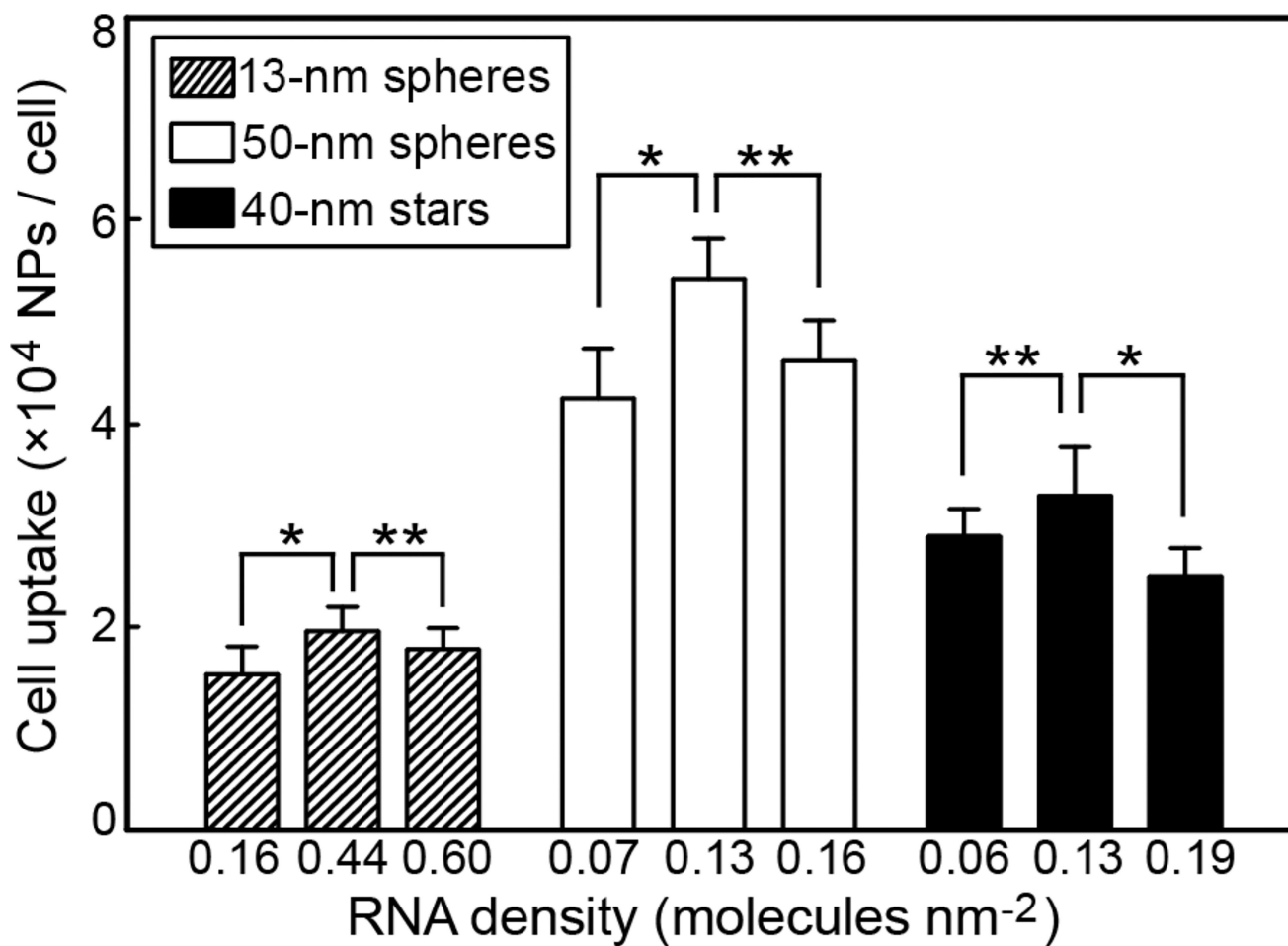
Figure 2.
Tunable loading of RNA strands on AuNPs by adjusting the molar ratio of siRNA to AuNP used for conjugation. S and AS represent sense and anti-sense strands, respectively.
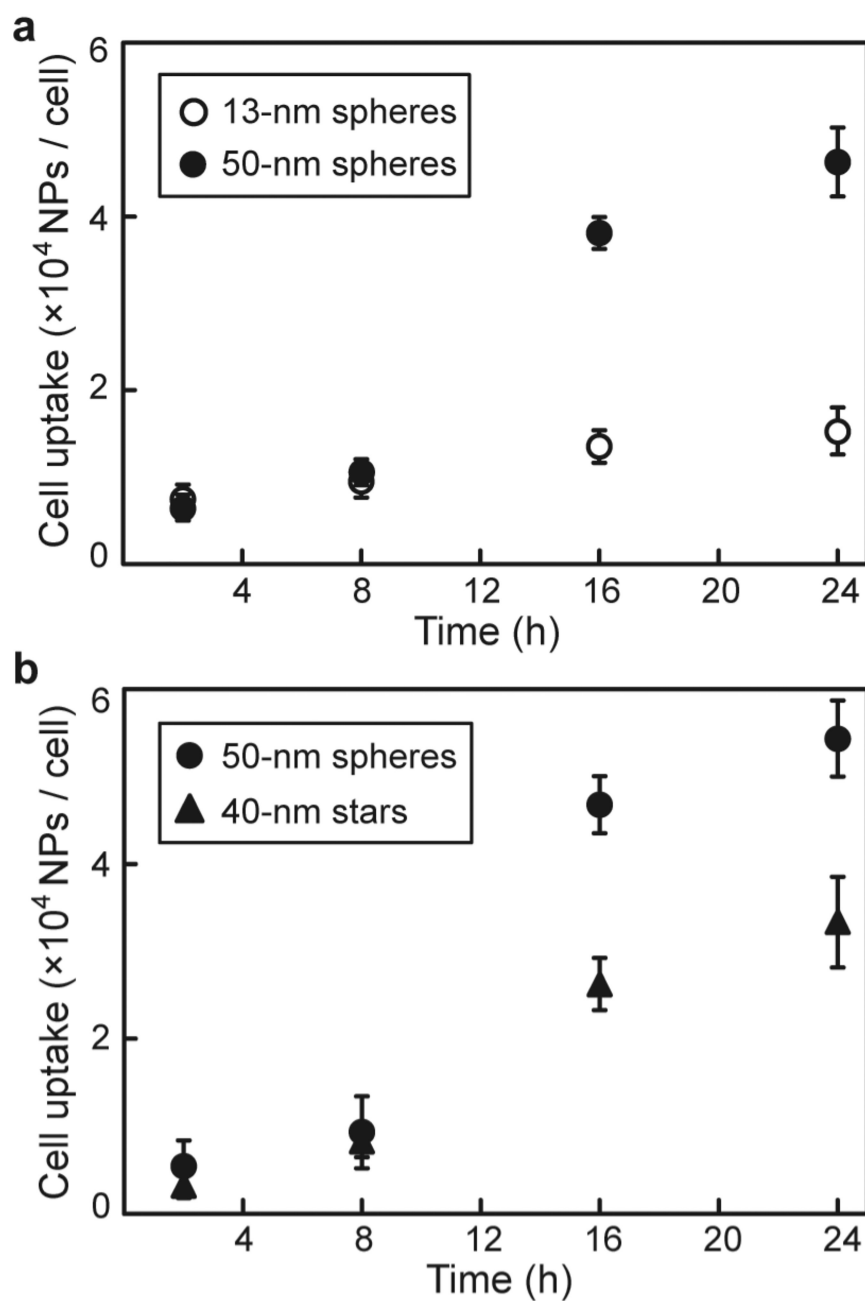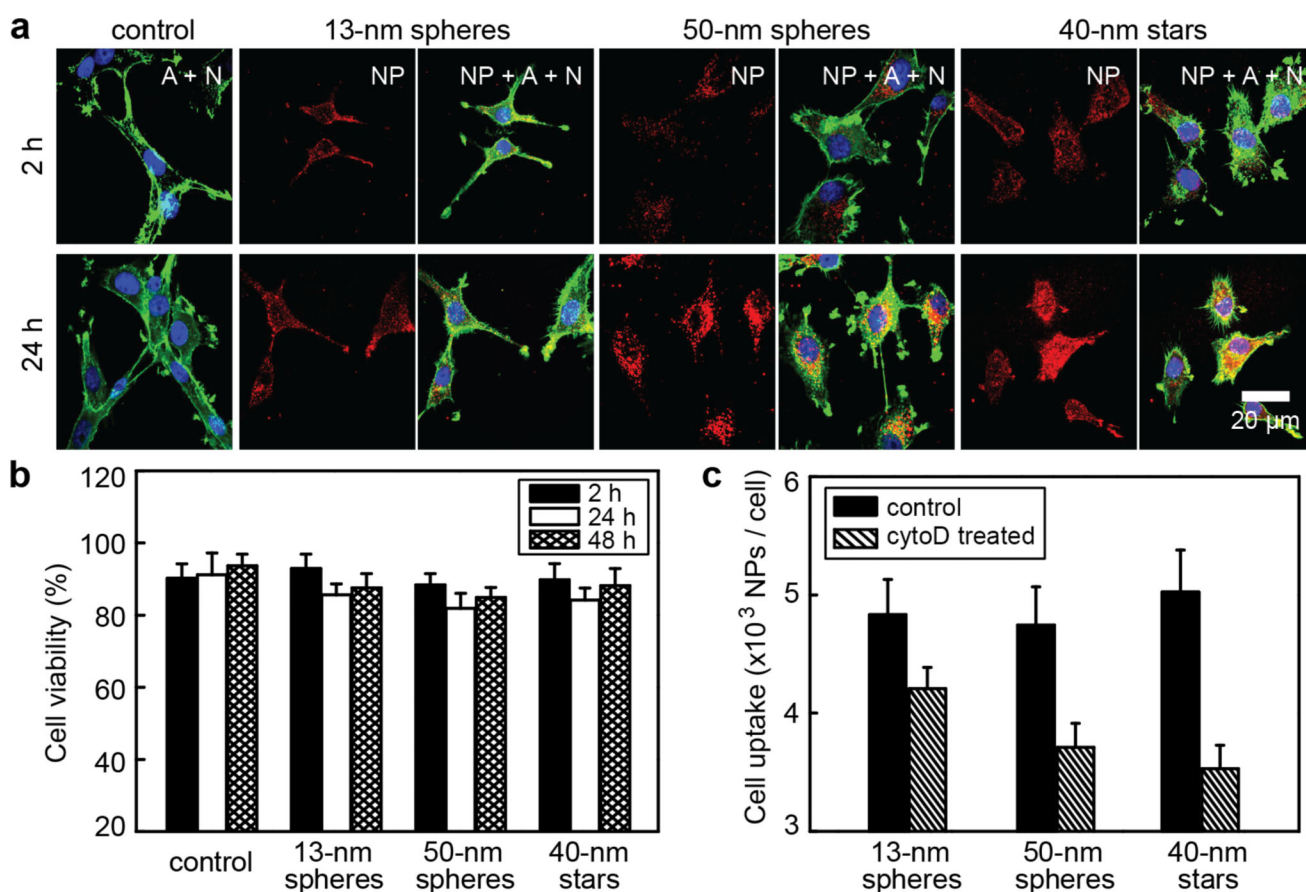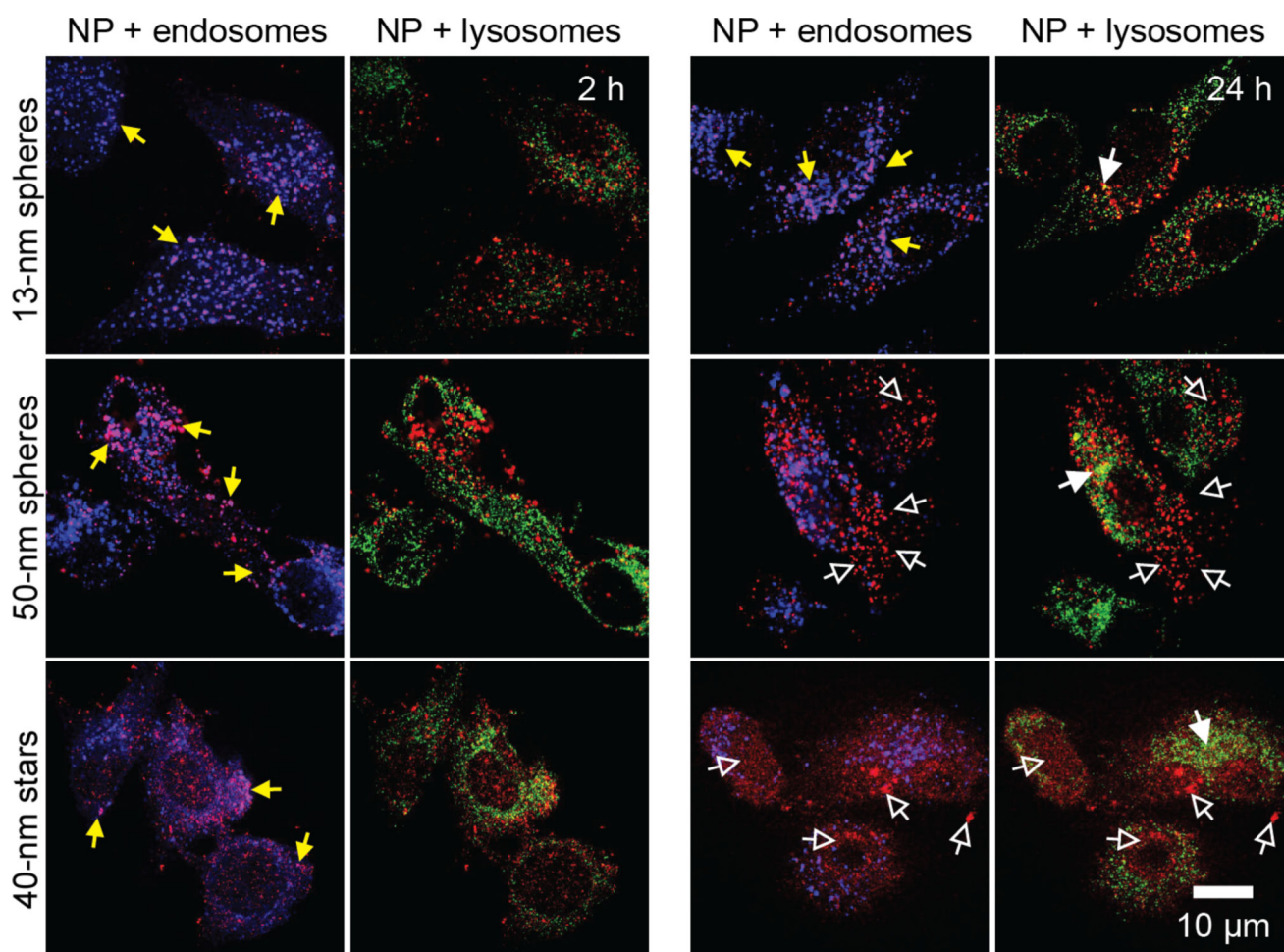
Figure 3.
(a) Size- and **(b)** shape-dependent cellular uptake kinetics of Au NP-siRNA constructs. In (a), 13-nm spheres (23 ± 8 AS per NP) and 50-nm spheres (329 ± 42 AS per NP) had similar oligonucleotide densities of ~ 0.16 molecules nm^{-2}. In (b), 50-nm spheres (221 ± 34 AS per NP) and 40-nm stars (251 ± 41 AS per NP) had oligonucleotide densities of ~ 0.13 molecules nm^{-2}.

Figure 4.
NP-siRNA constructs with median density of total RNA exhibited the highest cellular uptake efficiency (*$p < 0.05$; **$p > 0.05$).
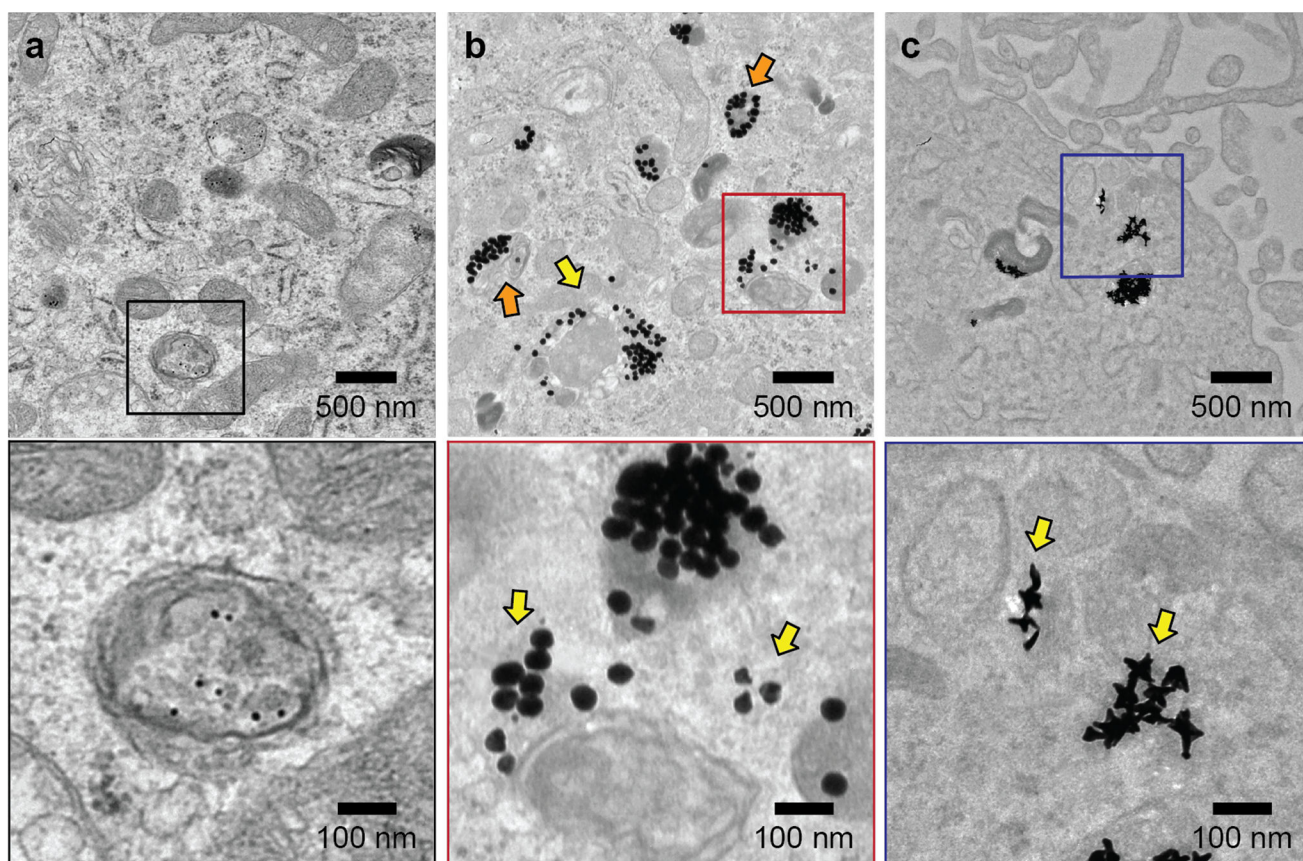
Figure 5.
Intracellular distribution of NP-siRNA constructs and cell morphology changes induced by larger constructs. (a) Confocal fluorescence images of cells treated with PBS (control) or three different formulations of constructs with the same concentration of NPs (0.2 nM); The actin (A) cytoskeleton and nucleus (N) were stained with Alexa Fluor® 594 Phalloidin (green) and DAPI (blue), respectively; nanoconstructs were labeled with Cy5 (red). The scale bar is 20 μm for all images. (b) MTS assay of the cell viabilities of U87 cells treated with three different formulations of NP-siRNA/Cy5 (0.2 nM) or PBS as the control; (c) Cell uptake inhibition by CytoD for three formulations. Following 30-min pre-treatment with CytoD, U87 cells were incubated with NP-siRNA in presence of CytoD for another 30 min and cell uptake was measured by ICP-MS. As a control, U87 cells were also treated with constructs under the same conditions, but without cytoD.

Figure 6.
Confocal fluorescent immunostaining studies indicate size- and shape-dependent subcellular localizations of NP-siRNA constructs. Cy5-labeled nanoconstructs (0.2 nM in NP, red color) were treated with U87 cells for 2 h or 24 h, followed by immunostaining of endosomes and lysosomes by EEA-1 antibody (blue) and LAMP-1 antibody (green), respectively. The solid yellow arrows indicate co-localizations of constructs with endosomes; solid white arrows indicate the co-localization of constructs with lysosomes; hollow white arrows indicate constructs that are neither localized in endosomes nor in lysosomes. The scale bar is 10 μm for all images.

Figure 7.
Representative TEM images of U87 cells after treatment with NP-siRNA constructs indicate
larger constructs can distribute in the cytoplasm. U87 cells were treated with 0.5 nM of **(a)**
13-nm spheres, **(b)** 50-nm spheres, and **(c)** 40-nm stars for 24 h. Images in boxes (lower
panel) indicate zoomed-in views. Yellow arrows indicate NPs distributed outside vesicles;
orange arrows indicate locally disrupted vesicle membranes.

Table 1

Characterizations of RNA functionalized gold nanoconstructs

core	SA (nm²)	# S / NP	# AS / NP	density #(S+AS) / nm²	size* (nm)	ζ-potential (mV)
13-nm spheres	531	60 ± 10	23 ± 8	0.16	29.2 ± 3.1	−28.8 ± 1.9
		151 ± 19	85 ± 8	0.44	29.7 ± 0.7	−31.6 ± 1.7
		208 ± 28	110 ± 10	0.60	32.0 ± 2.2	−35.2 ± 2.1
50-nm spheres	7840	397 ± 43	147 ± 12	0.07	72.0 ± 0.8	−34.2 ± 1.8
		780 ± 43	221 ± 34	0.13	63.9 ± 1.2	−35.5 ± 1.7
		962 ± 57	329 ± 42	0.16	64.3 ± 0.6	−31.0 ± 1.9
40-nm stars	7790	343 ± 35	122 ± 11	0.06	53.5 ± 0.4	−42.2 ± 1.1
		772 ± 39	251 ± 41	0.13	52.7 ± 1.1	−34.1 ± 1.7
		1071 ± 62	398 ± 56	0.19	50.4 ± 0.7	−39.0 ± 2.2

Surface area (SA) of 40-nm stars was estimated by methods using FITC-labeled PEG-SH (Supporting Information, Figure S1);

#
molecules of anti-sense (AS) and sense (S) strands per NP were determined by dissociating the oligonucleotides from AuNPs sequentially and quantifying each by analyzing the fluorescence of complexes of the strands with OliGreen;

*
hydrodynamic diameter was determined by dynamic light scattering (DLS)